Article | Open Access

Energy Materials

Peng *et al. Energy Mater.* **2026**, *6*, 600131 **DOI:**10.20517/energymater.2026.199

# Anion-participating solvation enables compositionally graded interphases for durable subzero lithium-ion batteries

**Shouxun Peng[1], Qing Yin[1,*], Bin Zhang[1], Zeyu Zhao[1], Meiyu Shi[1], Xiwen Li[1], Zheng Li[1], Bin Xiao[1], Xiuquan Gu[1], Mingjia Zhi[2], Eugene Chubenko[3], Vitaly Bondarenko[3], Hanna Bandarenka[3], Yang Pan[4], Shan Hua[4], Yanwei Sui[1,*]**

**Keywords:**
Electrolyte design, low-temperature lithium-ion batteries, solvation structure, depth-resolved interphase chemistry, long-cycle stability

**Citation:** Peng, S.; Yin, Q.; Zhang, B.; Zhao, Z.; Shi, M.; Li, X.; Li, Z.; Xiao, B.; Gu, X.; Zhi, M.; Chubenko, E.; Bondarenko, V.; Bandarenka, H.; Pan, Y.; Hua, S.; Sui, Y. Anion-participating solvation enables compositionally graded interphases for durable subzero lithium-ion batteries. *Energy Mater.* **2026**, *6*, 600131. https://dx.doi.org/10.20517/energymater.2026.199

**Received:** 1 Jul 2026
**First Decision:** 24 Jul 2026
**Revised:** 14 Aug 2026
**Accepted:** 31 Aug 2026
**Published:** 29 Sep 2026

**Academic Editor:** Yuping Wu
**Copy Editor:** Fangling Lan
**Production Editor:** Fangling Lan

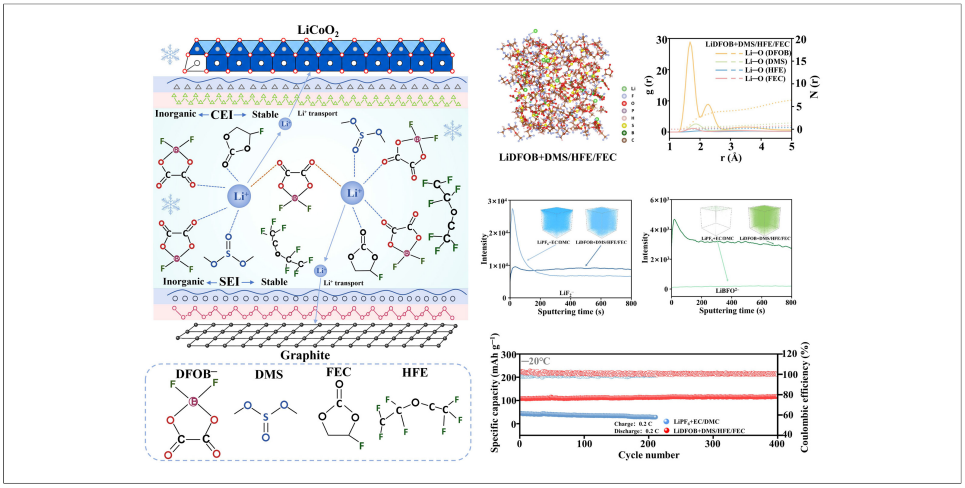


## Abstract

Low-temperature operation remains a critical bottleneck for lithium-ion batteries (LIBs), since the coupled limitations in $Li^+$ transport, desolvation and interfacial stability severely undermine energy delivery and long-term cyclability. Here, rather than merely relying on low-freezing-point solvents to improve electrolyte fluidity, we design a lithium difluoro(oxalato)borate (LiDFOB)-based electrolyte combining fluoroethylene carbonate (FEC), dimethyl sulfite (DMS) and 1,1,2,2-Tetrafluoroethyl-2,2,2-trifluoroethyl ether (HFE) to simultaneously regulate the solvation structure and interfacial reactions under subzero conditions. Molecular dynamics simulations reveal that the LiDFOB + DMS/HFE/FEC electrolyte reconstructs the $Li^+$ solvation sheath from solvent-dominated coordination in $LiPF_6$ + ethylene carbonate/dimethyl carbonate to an anion-dominated, aggregate-rich structure. Sputtering-time-dependent X-ray photoelectron spectroscopy reveals a compositionally graded graphite solid electrolyte interphase in which LiF remains the predominant fluorine-containing species and the relative contribution of Li-O-containing species increases with continued sputtering, while total-ion-normalized time-of-flight

[1]School of Materials and Physics, China University of Mining and Technology, Xuzhou 221116, Jiangsu, China.
[2]School of Materials Science and Engineering, Zhejiang University, Hangzhou 310058, Zhejiang, China.
[3]Belarusian State University of Informatics and Radioelectronics, Minsk 220013, Belarus.
[4]Guoneng Nanjing Electric Power Testing and Research Co., Ltd., Nanjing 210046, Jiangsu, China.

***Correspondence to:** Prof. Qing Yin, Prof. Yanwei Sui, Jiangsu Province High-efficiency Energy Storage Technology and Equipment Engineering Laboratory, School of Materials Science and Physics, China University of Mining and Technology, Xuzhou 221116, Jiangsu,

China. E-mail: qingyin0715@cumt.edu.cn; suiyanwei@cumt.edu.cn

secondary ion mass spectrometry provides complementary semiquantitative trends for selected interphase fragments. A compositionally differentiated hybrid cathode interphase containing borate-related components and reduced organic accumulation is also observed on $LiCoO_2$. As a result, $LiCoO_2$||Li cells using the LiDFOB-based electrolyte retain 93.77% of the initial discharge capacity after 500 cycles at 1.0 C and 25 °C. Even at -20 °C, they deliver 139.6 mAh $g^{-1}$ and retain 132.8 mAh $g^{-1}$ after 500 cycles at 0.2 C, corresponding to 95.1% retention. Meanwhile, $LiCoO_2$||graphite full cells also exhibit markedly improved cycling stability at -20 °C, delivering 116.8 mAh $g^{-1}$ after 400 cycles at 0.2 C. Rather than optimizing solvation structure or interphase chemistry in isolation, this work links anion-involved $Li^+$ coordination to depth-dependent interfacial evolution and identifies solvation-to-interphase coupling as a practical design principle for extending the cycling life of low-temperature LIBs.

## INTRODUCTION

Lithium-ion batteries (LIBs) have become the dominant power source for portable electronics and electric vehicles, and are increasingly deployed in large-scale grid storage enabled by their high energy density and extended cycle life[1-3]. However, their widespread adoption in high-latitude regions, aerospace and high-altitude applications is severely hampered by a sharp decline in both power capability and energy efficiency at subzero temperatures[4-6]. This performance degradation originates from two coupled kinetic limitations that become increasingly severe as temperature drops, namely higher bulk electrolyte resistance that impedes ionic transport, and sluggish interfacial charge-transfer kinetics that amplify polarization and reduce accessible capacity[7]. More critically, prolonged low-temperature operation can destabilize the electrode-electrolyte interphases, leading to continuous loss of cyclable lithium and accelerating capacity decay over long cycling[8,9].

Addressing these intertwined limitations requires a holistic electrolyte design strategy that can simultaneously mitigate bulk transport resistance, reduce interfacial desolvation penalties, and construct interphases resilient enough for prolonged low-temperature operation. As temperature decreases, increased electrolyte viscosity leads to a reduction in ionic conductivity, impeding $Li^+$ migration in the bulk electrolyte and intensifying ohmic polarization[10]. Furthermore, the $Li^+$ desolvation process at the electrode-electrolyte interface becomes significantly hindered at low temperature because solvent and anion coordination must be disrupted prior to charge transfer and insertion, thereby imposing an activation barrier that becomes more consequential upon cooling[11,12]. Accordingly, $Li^+$ desolvation and subsequent transport across the interphase are widely regarded as rate-limiting steps during low-temperature intercalation, particularly for graphite anodes, where $Li^+$ must first traverse a compact solid electrolyte interphase (SEI) before insertion[13]. This dual requirement, balancing kinetics with interfacial stability, poses a fundamental challenge to conventional carbonate-based electrolytes (e.g., $LiPF_6$ in ethylene carbonate (EC)/dimethyl carbonate (DMC)), which typically form solvent-derived, organic-rich SEI layers with limited mechanical robustness and relatively low ionic conductivity, thereby amplifying interfacial resistance and accelerating capacity loss during low-temperature cycling[14,15]. In addition, the intrinsic instability of $LiPF_6$ further aggravates these limitations. It is highly susceptible to hydrolysis and decomposition, generating reactive species such as $PF_5$ and HF, which not only corrode electrode surfaces but also accelerate the dissolution of transition metals from the cathode, thereby triggering degradation processes that undermine both interphase integrity and bulk electrode stability[16,17].

To mitigate these limitations, recent advances have established molecular-level electrolyte design as a powerful approach for coordinating low-temperature molecular mobility and ion-solvent interactions[18-20]. More recently, temperature-adaptive fluorine chemistry in weakly solvating sulfonamide electrolytes has

promoted the formation of conductive $LiF_x$-containing interphases and sustained lithium-metal battery operation at -30 °C[21]. Meanwhile, weakly coordinating fluorinated and sulfonamide-based solvents have been explored to reshape solvation environments toward contact ion pairs (CIP) and aggregate-rich structures, thereby promoting inorganic-rich interphases and reducing interfacial polarization during low-temperature operation[22,23]. Although these strategies improved the rate capability and energy output of LIBs at low temperature, sustaining such performance over prolonged cycling remains a formidable challenge because interfacial stability and electrode integrity become increasingly critical under these conditions. Extensive studies have demonstrated that regulating the $Li^+$ solvation structure is an effective way to couple bulk ion transport with interphase formation, especially at low temperatures where the desolvation process and subsequent interfacial reactions increasingly govern the overall cell kinetics and stability[24]. By modulating the relative binding affinities among solvent molecules, $Li^+$ and anions, the primary solvation sheath can be engineered to favor anion participation. This shift in coordination fundamentally alters the interfacial decomposition chemistry and can steer the SEI and cathode-electrolyte interphase (CEI) formation toward different compositional pathways[25]. Among promising lithium salts, lithium difluoro(oxalato)borate (LiDFOB) offers the borate- and fluorine-containing anion chemistry that can favor inorganic-rich interphase formation while avoiding $PF_6$-derived reaction pathways often associated with interphase instability[26]. Importantly, the $DFOB^-$ anion exhibits a stronger tendency to coordinate with $Li^+$ and this tendency becomes more pronounced when solvent donor strength is moderated, which promotes anion participation in the solvation sheath and can lower the reliance on solvent-dominated coordination at low temperature[27]. Furthermore, the reductive decomposition of LiDFOB can yield a hybrid inorganic matrix composed of LiF and boron-containing species (e.g., borates). Such inorganic-rich frameworks can combine mechanical resilience to withstand electrode volume changes and sufficient $Li^+$ conductivity to facilitate interfacial charge transfer, which is particularly beneficial for stable low-temperature cycling[28,29].

Beyond lithium salt selection, the design of the solvent plays an equally pivotal role, governing the thermodynamics of $Li^+$ solvation and dictating transport properties at low temperatures, which in turn fundamentally shapes the chemistry of the resulting interphases. Conventional carbonate solvents, owing to their strong solvating power, effectively promote salt dissociation and ensure high ionic conductivity at ambient temperature. However, this strong coordination reinforces $Li^+$-solvent interaction within the primary solvation sheath, thereby elevating the energetic penalty for interfacial desolvation, which becomes prohibitively severe as the temperature drops[30]. By contrast, weakly coordinating solvents can attenuate $Li^+$-solvent binding, whereas low-viscosity co-solvents can improve bulk transport, both of which become increasingly beneficial as temperature decreases[31]. Fluorinated solvents or diluents can further reshape interfacial reactivity by biasing reductive decomposition toward fluoride-rich inorganic motifs while simultaneously depressing the formulation's freezing point to preserve fluidity[32]. Therefore, salt chemistry and solvent engineering must be integrated so that bulk conductivity, desolvation kinetics and interfacial robustness can be optimized in a cooperative manner rather than traded off independently. Nevertheless, the mechanistic linkage among anion-involved solvation, depth-dependent interphase organization in the SEI and CEI, and sustained long-term cycling stability at low temperature remains insufficiently understood. In particular, how salt chemistry and solvent coordination jointly regulate interphase composition across different depths while maintaining low-temperature electrochemical durability remains largely unexplored.

Rather than optimizing solvation or interphase chemistry in isolation, this work connects solvation regulation with depth-dependent interphase evolution and uses this coupling as a design principle for low-temperature durability. Herein, we report a rationally designed electrolyte, comprising LiDFOB as the key salt, along with FEC, DMS and HFE as co-solvents, that simultaneously addresses the coupled demands of bulk transport, interfacial kinetics and interphase stability for long-cycling, low-temperature LIBs. The choice of DMS and HFE is important because DMS helps modulate $Li^+$ coordination and reduce the

dominance of solvent-controlled interfacial reactions, while HFE preserves fluidity without strongly coordinating $Li^+$. Meanwhile, HFE acts as an inert fluorinated diluent that preserves bulk fluidity at subzero temperatures without significantly disturbing the anion-involved solvation structure. This salt and solvent combination reshapes the $Li^+$ solvation sheath toward stronger anion participation and steers interfacial reactions toward a graded graphite SEI enriched in LiF, Li-O-containing species, and borate-related components, together with a compositionally graded hybrid CEI on the $LiCoO_2$ cathode. These interphase features help reconcile the inherently conflicting demands of low-temperature kinetics and long-term interfacial stability, as elucidated by systematic depth-profiling X-ray photoelectron spectroscopy (XPS) and time-of-flight secondary ion mass spectrometry (TOF-SIMS) analyses. This synergistic stabilization translates into outstanding electrochemical performance, as the $LiCoO_2$||Li cell with a LiDFOB-based electrolyte achieves a capacity retention of 95.1% after 500 cycles at 0.2 C and -20 °C. In contrast, the conventional $LiPF_6$-based carbonate electrolyte exhibits severe capacity degradation at -20 °C and fails much earlier during cycling. Moreover, the $LiCoO_2$||graphite exhibits gradual activation during cycling at -20 °C, with its discharge capacity increasing from 108.1 mAh $g^{-1}$ in the first cycle to 116.8 mAh $g^{-1}$ after 400 cycles at 0.2 C. Collectively, these results show that solvation regulation and interphase chemistry must be engineered in a coordinated manner, since low-temperature durability is ultimately dictated by the coupled effects of $Li^+$ solvation structure and the resultant electrode-electrolyte interphases.

## EXPERIMENTAL

### Electrode preparation

Commercial $LiCoO_2$ ($D_{50}$ = 6 μm, 99.5%) and graphite powder (NF-A, 99.5%) were purchased from Ningbo Chuangli New Material Technology Co., Ltd. and used as received. The $LiCoO_2$ cathode slurry was prepared by dispersing $LiCoO_2$ (75 wt%), poly(vinylidene fluoride) (PVDF, 15 wt%, Solef 5130, Solvay), and Super C65 carbon black (10 wt%, Imerys) in N-methyl-2-pyrrolidone (NMP) to form a homogeneous suspension. The slurry was doctor-bladed onto 18 μm aluminum foil (Showa Denko, Japan) with a wet thickness of 200 μm. Graphite anodes were fabricated by dispersing graphite powder (75 wt%), PVDF (15 wt%, Solef 5130, Solvay), and Super C65 carbon black (10 wt%, Imerys) in NMP to form a homogeneous suspension. The slurry was doctor-bladed onto copper foil with a wet thickness of 50 μm. All electrodes were dried under dynamic vacuum at 100 °C for 8 h and subsequently punched into disks (12 mm for cathodes and 14 mm for anodes) before cell assembly.

### Electrolyte formulation

The LiDFOB + DMS/HFE/FEC electrolyte was formulated by dissolving 1.5 M LiDFOB (99.9%) in a mixed solvent of DMS (99%), HFE (99.8%, battery grade), and FEC (99.9%, battery grade) with a volume ratio of 5:4:1 (v/v/v). DMS and $LiBF_4$ were purchased from Aladdin (China), while the remaining solvents were obtained from Dodo Chem Co., Ltd. (China). For comparison, a commercial carbonate electrolyte (LB-063, 1.0 M $LiPF_6$ in EC/DMC = 3:7, v/v) was purchased from Dodo Chem Co., Ltd. (China) and used as the reference electrolyte. The detailed compositions of all electrolyte formulations investigated in this work are summarized in Supplementary Table 1. (The reported molar concentration was defined as the number of moles of lithium salt divided by the final electrolyte volume measured after complete salt dissolution at 25 °C).

### Electrochemical measurements

CR2032-type $LiCoO_2$||Li half cells and $LiCoO_2$||graphite full cells were assembled in an Ar-filled glovebox ($H_2O$ and $O_2$ < 0.01 ppm, Universal series, Mikrouna (Shanghai) Industrial Intelligent Technology Co., Ltd., China) using a PP separator (Celgard 2400). After assembly, the cells were rested for 12 h to ensure complete wetting and then equilibrated at the target temperature in a programmable chamber (-60 to 120 °C, JD-8002-80L, Dongguan Jiedong Test Equipment Co., Ltd.) before electrochemical testing. $LiCoO_2$||Li half cells were used to evaluate the intrinsic electrochemical behavior of the $LiCoO_2$ electrode and electrolyte

compatibility. The half cells were tested within a voltage range of 2.8-4.2 V at both 25 and -20 °C. Cycling tests were performed at 1.0 C at 25 °C and 0.2 C at -20 °C based on the active $LiCoO_2$ mass. $LiCoO_2$||graphite full cells were assembled to evaluate practical battery performance. The graphite and $LiCoO_2$ electrodes had active-material loadings of 0.8-1.0 and 1.6-1.8 mg $cm^{-2}$, respectively. Based on nominal reversible specific capacities of approximately 300 mAh $g^{-1}$ for graphite and 140 mAh $g^{-1}$ for $LiCoO_2$, these loadings corresponded to areal capacities of approximately 0.24-0.30 and 0.22-0.25 mAh $cm^{-2}$, respectively. Electrodes within these loading ranges were matched to maintain a nominal N/P capacity ratio of approximately 1.1. Each full cell contained 120 μL of electrolyte. The electrolyte-to-capacity ratio of approximately 420-475 μL $mAh^{-1}$ was calculated by dividing the electrolyte volume by the nominal $LiCoO_2$ capacity. After assembly, the cells were rested for 12 h and equilibrated at the intended testing temperature. Cells evaluated at 25 and -20 °C were then formed at their respective testing temperatures by five cycles at 0.05 C before long-term cycling. At least five independently assembled full cells were tested for each electrolyte-temperature condition. Unless otherwise specified, the cycling curves show representative individual-cell results and are not averaged traces. Galvanostatic charge/discharge measurements were performed using a Neware BTS-4000 battery tester (Neware Technology Co., Ltd., China). The theoretical specific capacity corresponding to the complete extraction of one Li per $LiCoO_2$ formula unit is 274 mAh $g^{-1}$. Accordingly, 1 C was defined as a current density of 274 mA $g^{-1}$. All specific capacities were calculated based on the mass of active $LiCoO_2$ material.

## Characterization

Raman spectra were collected at -20 and 25 °C using a DXR2xi Raman spectrometer (DXR2xi, Thermo Fisher Scientific, USA) equipped with a 785 nm laser excitation. The surface morphologies of pristine and cycled electrodes were examined by a field-emission scanning electron microscope (FE-SEM, SU8220, Hitachi High-Tech Corporation, Japan). SEM images were acquired at an accelerating voltage of 5 kV and a beam current of 10 μA. XPS was performed on a VersaProbe 4 X-ray photoelectron spectrometer (PHI VersaProbe 4, ULVAC-PHI, Inc., Japan) with Al Kα radiation (1,486.6 eV) to probe surface chemical states and interphase compositions of the electrodes. Under the applied sputtering conditions, calibration against a certified $Ta_2O_5$ thin-film standard yielded a nominal $Ta_2O_5$-equivalent sputtering rate of approximately 0.3 nm $s^{-1}$. For XPS analysis of the uncycled LiDFOB + DMS/HFE/FEC and $LiPF_6$ + EC/DMC formulations, 20 μL of each electrolyte was drop-cast onto an identically sized, cleaned Cu-foil substrate inside an Ar-filled glovebox. The samples were transferred to the XPS load-lock in an airtight vessel without exposure to ambient air, and most volatile solvent components were removed during evacuation at room temperature. After the chamber pressure stabilized, the resulting electrolyte-derived residue films were analyzed using a PHI VersaProbe 4 instrument. Identical electrolyte volumes, substrate areas, evacuation procedures, and acquisition conditions were used for both formulations. Binding energies were referenced to the adventitious C 1s peak at 284.8 eV. TOF-SIMS measurements were carried out on a TOF-SIMS 5 instrument (TOF.SIMS 5, IONTOF GmbH, Germany) to obtain depth-resolved and three-dimensional chemical maps of the electrode interphases. The three-dimensional secondary-ion distributions were reconstructed using SurfaceLab software supplied by IONTOF GmbH. The corresponding total-ion-normalized sputtering-time profiles were plotted using OriginPro software supplied by OriginLab Corporation. For each sputtering cycle, the signal intensity of each selected secondary ion fragment was normalized to the total secondary ion counts collected during the same cycle. The resulting intensity profiles were used for semiquantitative comparison of the depth-dependent distributions of the selected fragments. Under the identical Cs source operating parameters as those used for the sample, sputter calibration was performed using a standard thin-film sample of known thickness to obtain a stable sputter rate.

### Theoretical calculations and molecular simulations

Molecular dynamics (MD) simulations were performed using LAMMPS (2023 release). The simulation box for the $LiPF_6$ electrolyte contained 10 $LiPF_6$ formula units, 37 EC molecules and 71 DMC molecules. The LiDFOB-based electrolyte model consisted of 10 LiDFOB formula units, 14 FEC molecules, 26 HFE molecules and 59 DMS molecules, and all components were described using the OPLS-AA force field. Simulations were carried out at 298.15 K with a 1 fs timestep. After adequate equilibration (including density relaxation when applicable), production trajectories were collected for statistical analysis. Radial distribution function (RDF) and coordination numbers between $Li^+$ ions and anions/solvent molecules species were computed from equilibrated production trajectories, with coordination numbers obtained by integrating RDFs to the first minimum. Accordingly, the reported values describe the average numbers of the selected atoms within the corresponding $Li^+$ coordination shells rather than the absolute numbers of molecular species surrounding each $Li^+$. The distribution of characteristic solvation motifs, including CIP, aggregates (AGG) and solvent-separated ion pairs (SSIP), was quantified using distance-based criteria defined from the $Li^+$-anion RDF. The MD simulation snapshots and the representative $Li^+$ solvation configurations shown in Supplementary Figure 1 were rendered using Visual Molecular Dynamics software. Quantum chemical calculations on the relevant electrolyte molecules were performed using Gaussian 09 to evaluate the frontier molecular orbitals. Geometry optimizations were conducted at the B3LYP/6-311+G(d,p) level, and the highest occupied molecular orbital (HOMO) and lowest unoccupied molecular orbital (LUMO) energies were extracted from the optimized structures. The corresponding frontier-orbital isosurfaces were rendered using GaussView 6.

## RESULTS AND DISCUSSION

Designing low-temperature electrolytes for LIBs necessitates a synergistic balance among low viscosity, depressed freezing/melting points, high ionic conductivity and sufficient salt dissociation. Molecular orbital energy calculations [Figure 1A] indicate that LiDFOB and FEC possess comparatively LUMO energies compared to the other electrolyte components, suggesting that they are more susceptible to reduction and can preferentially initiate interphase formation on the anode during initial cycles. Such preferential reduction is expected to form an inorganic-enriched SEI that facilitates rapid $Li^+$ transport and effectively passivates the anode against continuous electrolyte decomposition. Conversely, HFE exhibits a low-lying HOMO together with a relatively high LUMO, confirming its enhanced oxidative and reductive stability, which supports its function as an electrochemically inert diluent in the formulation. Simultaneously, the very low freezing points of DMS (-114 °C) and HFE (-91 °C) help maintain electrolyte fluidity at deeply subzero temperatures[33]. Therefore, the reductively labile LiDFOB and FEC are expected to promote LiF- and borate-enriched interphase chemistry, whereas the low-freezing-point co-solvents DMS and HFE help preserve electrolyte mobility at low temperatures, jointly improving interfacial stability and maintaining facile ion-transport kinetics under cold conditions. MD simulations [Figure 1B and C] combined with RDF analysis [Figure 1D and E] reveal pronounced differences in $Li^+$ solvation structure between the conventional carbonate electrolyte ($LiPF_6$ + EC/DMC) and the proposed LiDFOB-based new formulation (LiDFOB + DMS/HFE/FEC). In the $LiPF_6$ + EC/DMC system, $Li^+$ is primarily coordinated by the carbonyl oxygens of EC and DMC within its first solvation shell, while $PF_6^-$ anions show only a weak but discernible $Li^+$ correlation. The LiDFOB-based electrolyte exhibits a reconstructed $Li^+$ solvation environment characterized by a pronounced first-shell Li-O($DFOB^-$) correlation. Together with the increased CIP and AGG fractions, this distribution is consistent with enhanced participation of $DFOB^-$ in the $Li^+$ solvation environment. This shift towards an anion-coordinated solvation structure is anticipated to reshape the interfacial desolvation step and can mitigate low-temperature kinetic limitations by reducing the prevalence of solvent-dominated $Li^+$ coordination[34]. Furthermore, it steers the reductive decomposition pathway towards the formation of anion-derived, LiF-rich interphases, which are widely associated with long-term cycling stability. Figure 1F summarizes the atom-based Li-O coordination numbers and the Li-P($PF_6^-$) center-contact number obtained

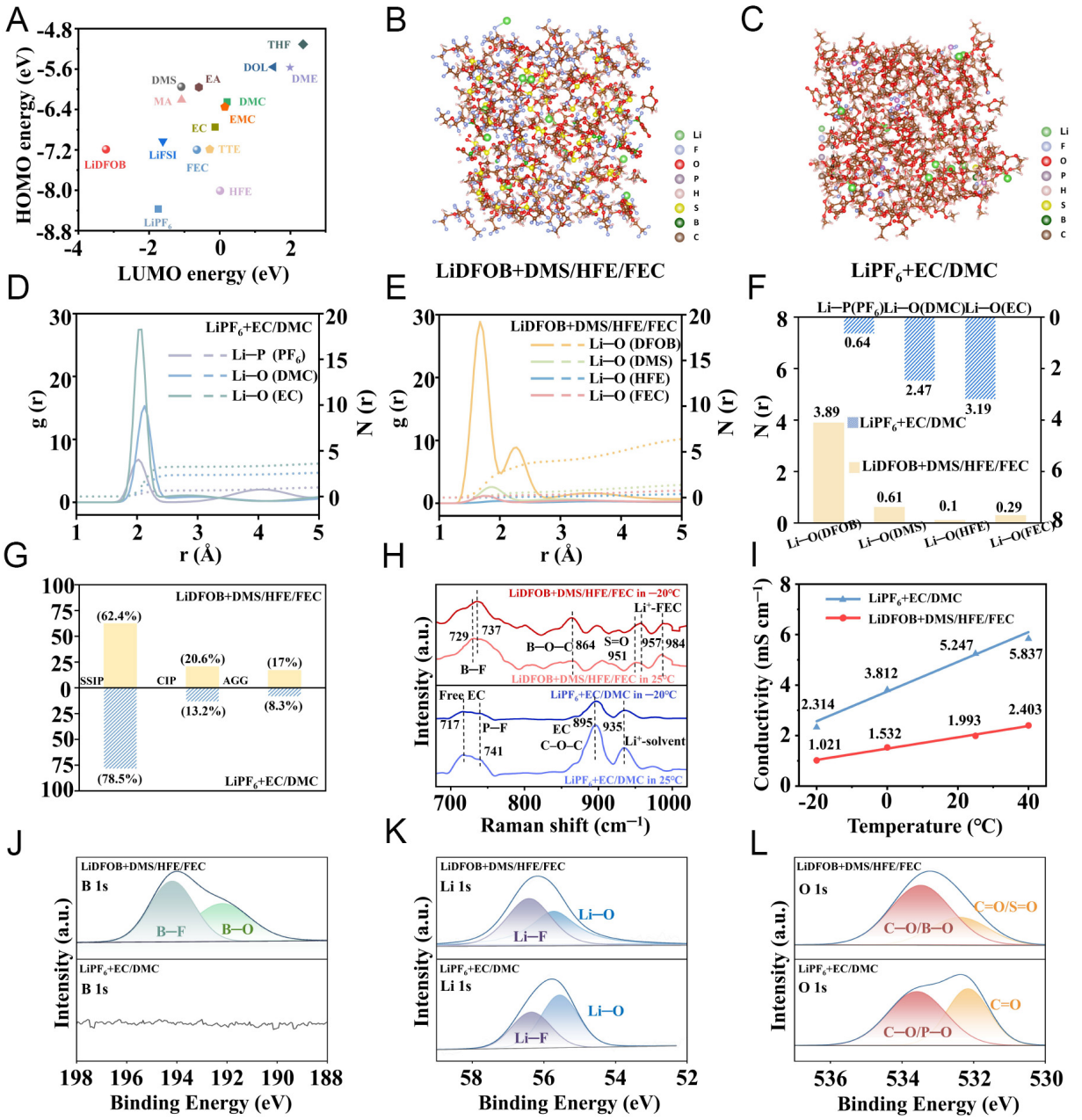


**Figure 1.** (A) Calculated HOMO and LUMO energy levels of the main electrolyte components. (B and C) MD simulation snapshots of $Li^+$ solvation structures. RDFs of (D) $LiPF_6$ + EC/DMC and (E) LiDFOB + DMS/HFE/FEC electrolytes. (F) Coordination numbers of LiDFOB + DMS/HFE/FEC and $LiPF_6$ + EC/DMC electrolytes. (G) The percentages of SSIPs, CIPs, and AGGs. (H) Raman spectra of both electrolytes at different temperatures. (I) Ionic conductivity as a function of temperature. (J-L) B 1s, Li 1s and O 1s XPS spectra of vacuum-treated electrolyte-derived residue films prepared from the two formulations.

by integrating the corresponding RDFs to their pair-specific first minima. In the $LiPF_6$ + EC/DMC electrolyte, the Li-O(EC) and Li-O (DMC) coordination contributions are 3.19 and 2.47, respectively, whereas the Li-P($PF_6^-$) center-contact number is 0.64, supporting predominantly solvent-associated $Li^+$ coordination in the conventional carbonate electrolyte. In sharp contrast, the LiDFOB + DMS/HFE/FEC electrolyte exhibits a markedly reconstructed $Li^+$ coordination environment, where the coordination contribution obtained from $Li^+$-O(DFOB) RDF integration reaches 3.89, far exceeding those of Li-O(DMS), Li-O(HFE) and Li-O(FEC), which are only 0.61, 0.10 and 0.29, respectively. Together with the increased CIP and AGG fractions shown in Figure 1G, these results support enhanced $DFOB^-$ participation and reduced solvent contribution in the $Li^+$ solvation environment.

Consistent with the RDF trends, ion-pair speciation statistics further reveal distinct solvation states for the two electrolytes [Figure 1G and Supplementary Figure 1]. Specifically, the LiDFOB + DMS/HFE/FEC formulation manifests increased proportions of CIPs (increased by 1.56 times) and aggregated ion clusters (AGG, increased by 2.05 times), accompanied by a concomitant decrease in SSIPs from 78.5% to 62.4%, compared to the baseline carbonate electrolyte. These speciation changes suggest more anion-associated $Li^+$ species and fewer free solvent molecules, which can alleviate solvent-dominated interfacial kinetics and support improved low-temperature performance. Figure 1H compares the temperature-dependent Raman spectra of the two electrolytes and reveals a distinct evolution of $Li^+$ solvation and ion-association structures upon cooling. At 25 °C, the Raman spectrum of the LiDFOB + DMS/HFE/FEC electrolyte exhibits characteristic bands at 729 $cm^{-1}$ (attributed to B-F vibration from $DFOB^-$) and 951 $cm^{-1}$ (assigned to the S=O-related mode of DMS)[35], together with additional features in the 850 to 1,000 $cm^{-1}$ region. As the temperature decreases, both bands shift to higher wavenumbers, from 729 to 737 $cm^{-1}$ and from 951 to 957 $cm^{-1}$, respectively [Supplementary Figure 2]. Such upshifts reflect a temperature-induced change in the local bonding environment, consistent with strengthened $Li^+$ coordination and enhanced ion association at subzero temperature, also in line with the speciation trends extracted from MD and RDF analyses. By contrast, $LiPF_6$ + EC/DMC shows only minor peak-position changes upon cooling, yet the overall Raman intensities decrease noticeably at -20 °C, signifying restricted molecular mobility and increased local viscosity observed in Supplementary Figure 3, which can foreshadow mass-transport limitations at low temperature. Additional salt-controlled comparisons under identical DMS/HFE/FEC solvent conditions further verify that the reconstructed anion-involved coordination environment originates from the specific chemistry of $DFOB^-$ rather than solely from the increased salt-to-coordinating-solvent ratio induced by HFE dilution [Supplementary Figures 4 and 5]. Figure 1I compares the ionic conductivities of the two electrolyte systems at various temperatures. The conventional $LiPF_6$ + EC/DMC electrolyte exhibits ionic conductivities of 2.314, 3.812, 5.247 and 5.837 mS $cm^{-1}$ at -20, 0, 20 and 40 °C, respectively. For LiDFOB + DMS/HFE/FEC, the corresponding values are 1.021, 1.532, 1.993 and 2.403 mS $cm^{-1}$. Although the LiDFOB-based electrolyte shows lower bulk conductivity, it offers two coupled advantages that are particularly relevant for low-temperature cycling. Firstly, anion-reinforced coordination can bias the early-stage reduction chemistry toward inorganic-rich SEI components, which can improve mechanical integrity and help mitigate parasitic Li plating under low-temperature cycling [Supplementary Figure 6]. Meanwhile, the anion-involved clustered solvation structure shifts the kinetic bottleneck from bulk ion transport toward interfacial charge transfer. The less temperature-sensitive apparent interfacial resistance, together with the solvation and interphase analyses, indicates more favorable interfacial $Li^+$ transport that can partly compensate for the lower bulk ionic conductivity.

To compare the chemical compositions retained after evacuation, XPS measurements were performed on residue films derived from the LiDFOB + DMS/HFE/FEC and $LiPF_6$ + EC/DMC formulations using identical deposition, airtight transfer, and XPS load lock evacuation procedures. The survey spectra reveal clear formulation-dependent differences in the elemental signatures retained in the resulting residue films [Supplementary Figure 7]. In the residue film derived from the LiDFOB-based electrolyte, the B 1s spectrum contains two components centered at 194.2 eV (assigned to a B-F environment, indicative of fluoroborate-like motifs) and 192.1 eV (assigned to a B-O environment, consistent with borate/oxalate-derived species) [Figure 1J], consistent with the presence of boron-containing species originating from the LiDFOB salt. As expected, no B 1s signal is detectable in the residue film derived from the B-free $LiPF_6$ + EC/DMC formulation, confirming the specificity of the boron features to the LiDFOB-based formulation. The Li 1s spectra of both residue films can be deconvoluted into two peaks located at 55.5 and 56.3 eV, corresponding to Li-O and Li-F-related chemical states, respectively [Figure 1K]. However, the relative contribution of the Li-F component is markedly greater in the residue film derived from LiDFOB + DMS/HFE/FEC. This enhancement indicates a higher relative abundance of Li-F-related species retained in the LiDFOB-based

residue film after vacuum treatment and provides complementary information regarding the distinct chemical compositions of the two formulations. In the O 1s spectra [Figure 1L], the LiDFOB-based residue film displays components near 532.3 and 533.5 eV that can be assigned to C=O or S=O and C-O or B-O environments, respectively, whereas the relative C=O contribution is markedly suppressed. This suppression of the carbonyl signal reflects the distinct oxygen-containing chemical states retained from the LiDFOB-based formulation after vacuum treatment. Collectively, these spectroscopic signatures demonstrate formulation-dependent differences in the chemical states retained within the electrolyte-derived residue films and complement the solvation trends independently revealed by MD simulations and Raman spectroscopy.

To evaluate the performance of the two electrolytes at both room and low temperatures, $LiCoO_2$||Li cells were assembled and their electrochemical profiles at 25 and -20 °C were systematically compared. Figure 2A and B shows the cyclic voltammetry (CV) responses of $LiCoO_2$||Li cells with LiDFOB + DMS/HFE/FEC and $LiPF_6$ + EC/DMC at 25 °C, respectively, over 2.8-4.2 V at scan rates of 0.1-0.5 mV $s^{-1}$. Both electrolytes exhibit well-defined redox peaks, and the peak currents increase progressively with increasing scan rate. Compared with $LiPF_6$ + EC/DMC, the LiDFOB + DMS/HFE/FEC electrolyte exhibits a higher current response, while the $LiPF_6$ + EC/DMC system shows relatively broader redox features. Nyquist plots [Figure 2C and D] reveal that the LiDFOB + DMS/HFE/FEC electrolyte possesses a markedly lower apparent interfacial resistance ($R_{int}$) at 25 °C. The LiDFOB + DMS/HFE/FEC electrolyte exhibits an approximately 11.7% lower $R_{int}$ than $LiPF_6$ + EC/DMC, indicating reduced resistance to interfacial $Li^+$ transport. More importantly, upon cooling to -20 °C, the $R_{int}$ of the LiDFOB + DMS/HFE/FEC electrolyte increases only modestly from 27.2 Ω at 25 °C to 38.9 Ω at -20 °C [Supplementary Figure 8], whereas the $LiPF_6$-based counterpart suffers 3.58-fold resistance amplification. Temperature-dependent impedance spectra and the corresponding Arrhenius analyses reveal that the apparent interfacial resistance increases upon cooling for both electrolytes [Supplementary Figures 9 and 10, Supplementary Tables 2 and 3 ]. The calculated apparent activation energies associated with the interfacial process are 8.9 and 20.6 kJ $mol^{-1}$ for the LiDFOB + DMS/HFE/FEC and $LiPF_6$ + EC/DMC electrolytes, respectively, indicating more favorable interfacial kinetics and reduced temperature sensitivity in the LiDFOB-based electrolyte. The matched-solvent $LiBF_4$ control exhibits a pronounced increase in apparent interfacial impedance upon cooling from 25 to -20 °C [Supplementary Figure 11]. This result indicates that the DMS/HFE/FEC solvent environment alone does not eliminate the temperature sensitivity of the interfacial process and that lithium-salt chemistry also contributes to the low-temperature kinetic response. Consistent with the kinetic advantages revealed by CV and electrochemical impedance spectroscopy (EIS), the LiDFOB + DMS/HFE/FEC enables exceptional cycling stability at 25 °C, retaining 93.77% of its initial discharge capacity (145.76 mAh $g^{-1}$) over 500 cycles at 1.0 C with Coulombic efficiency remaining above 99% in Figure 2E. In contrast, the $LiPF_6$ + EC/DMC system experiences progressive capacity fading under identical conditions, underscoring the superior interfacial stability conferred by the designed electrolyte. The low-temperature performance disparity is even more pronounced at -20 °C in Figure 2F. With LiDFOB + DMS/HFE/FEC electrolyte, the cell delivers an initial discharge capacity of 139.6 mAh $g^{-1}$ at -20 °C and retains 132.8 mAh $g^{-1}$ after 500 cycles at 0.2 C, corresponding to 95.1% retention, demonstrating significantly better low-temperature performance compared to traditional $LiPF_6$-based electrolyte, which only achieves 30.2 mAh $g^{-1}$ discharge capacity at -20 °C and fails within 200 cycles. This performance discrepancy stems from the anion-involved solvation structure of the LiDFOB + DMS/HFE/FEC electrolyte that biases interfacial reactions toward inorganic-rich interphase products with higher chemical robustness and improved $Li^+$ conductivity. Such a robust SEI effectively suppresses continuous solvent decomposition and promotes uniform $Li^+$ flux, thereby mitigating dendrite growth and supporting prolonged cycle life, particularly under the kinetically limited low-temperature conditions. This will be further supported by the interfacial analyses discussed later.

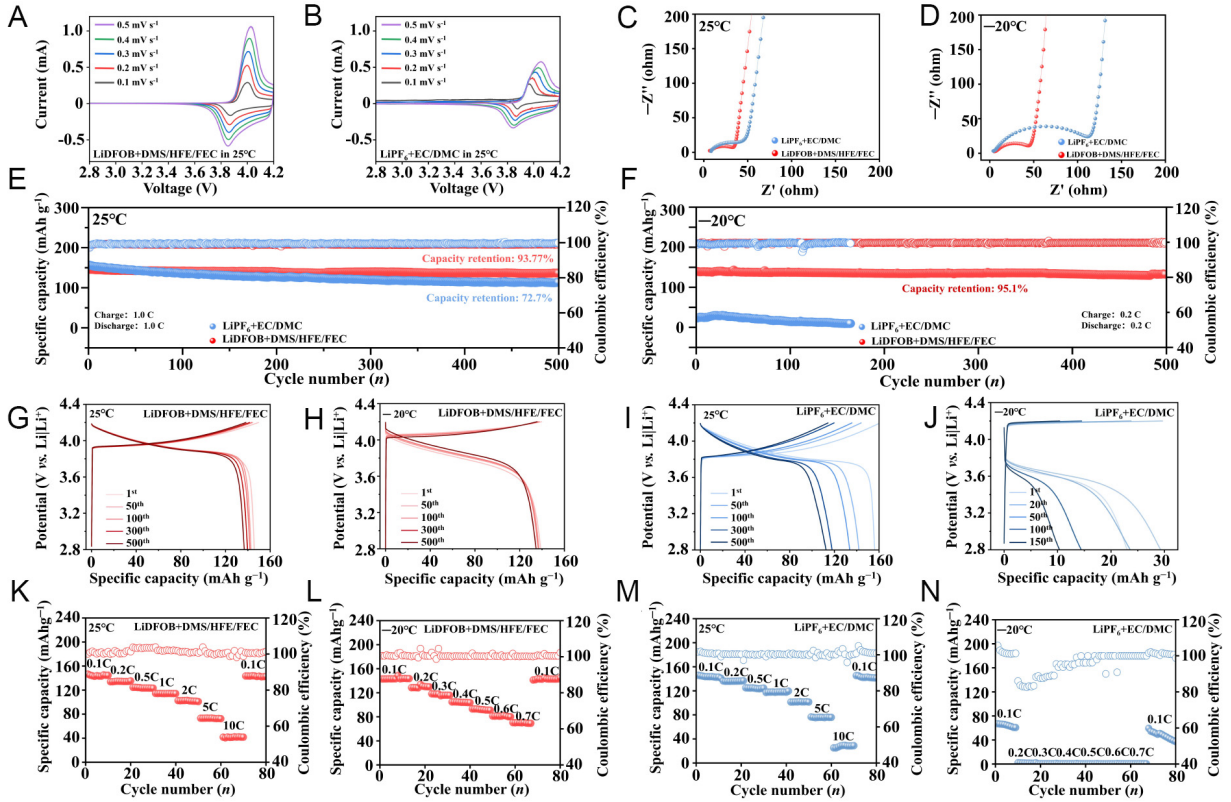


**Figure 2.** CV curves at 25 °C with different scan rates of (A) LiDFOB + DMS/HFE/FEC and (B) $LiPF_6$ + EC/DMC electrolytes. Nyquist plots at (C) 25 °C and (D) -20 °C. Long-term cycling performance of $LiCoO_2$||Li cells with different electrolytes at (E) 25 °C and (F) -20 °C. (G-J) Corresponding charge/discharge curves with LiDFOB + DMS/HFE/FEC and $LiPF_6$ + EC/DMC electrolytes at 25 and -20 °C. (K-N) Rate capability and corresponding Coulombic efficiency with different electrolytes at 25 and -20 °C.

As depicted in Figure 2G and H, the LiDFOB + DMS/HFE/FEC electrolyte exhibits highly overlapping galvanostatic charge/discharge curves during cycling at both 25 and -20 °C, with only minor shifts in plateau voltage and limited polarization growth. In contrast, the $LiPF_6$ + EC/DMC system shows an evident downward shift and broadening of the discharge plateaus with cycling in Figure 2I and J, suggesting aggravated kinetic limitations and gradual degradation of the interfacial layer. Particularly under low-temperature conditions, the carbonate-based electrolyte struggles to maintain stable and reversible plateaus, showing a significant voltage drop that reflects severely impeded interfacial kinetics upon cooling in the solvent-dominated solvation environment. This improved plateau stability and lower polarization with LiDFOB + DMS/HFE/FEC can be attributed to a more robust inorganic-rich interphase that provides persistent $Li^+$ transport pathways, consistent with its anion-involved coordination environment. Rate capability assessments at room temperature [Figure 2K] demonstrate that the LiDFOB + DMS/HFE/FEC system enables reversible capacities of 144.8, 134.7, 123.5, 114.1, 102.1, 72.6 and 46.4 mAh $g^{-1}$ at current rates of 0.1 C, 0.2 C, 0.5 C, 1 C, 2 C, 5 C and 10 C, respectively. Upon returning the current to 0.1 C after high-rate cycling, the capacity recovers to 143.4 mAh $g^{-1}$ with 99.03% capacity retention relative to the initial value, underscoring the excellent reversibility of the electrode processes and the structural integrity of the interphase under the designed electrolyte.

The rate performance of the LiDFOB + DMS/HFE/FEC electrolyte remains favorable under low-temperature conditions [Figure 2L]. At -20 °C, the cell maintains a reversible capacity of approximately 70.6 mAh $g^{-1}$ even at 0.7 C. When the current rate is restored to 0.1 C, the capacity recovers to 98.91% of its initial value, demonstrating the preserved reversibility of $Li^+$ transport and interfacial reaction processes under subzero

conditions. For comparison, the $LiPF_6$ + EC/DMC electrolyte exhibits comparable rate performance at 25 °C [Figure 2M], confirming that both electrolyte systems provide sufficient ionic transport under ambient conditions. However, a pronounced difference emerges at -20 °C [Figure 2N], where the $LiPF_6$ + EC/DMC cell suffers from severe kinetic limitations and cannot sustain stable operation even at a moderate rate of 0.2 C. These results demonstrate that the LiDFOB + DMS/HFE/FEC electrolyte effectively maintains low-temperature electrochemical kinetics despite its relatively lower bulk ionic conductivity. The enhanced performance originates from the synergistic regulation of ion transport and interfacial charge-transfer processes enabled by the anion-dominated solvation structure, thereby achieving superior rate capability and cycling stability under challenging thermal conditions.

Prior to the final electrolyte selection, different LiDFOB-based solvent combinations were compared in $LiCoO_2$||Li cells at -20 °C [Supplementary Figure 12], among which the LiDFOB + DMS/HFE/FEC formulation delivered the most stable cycling behavior and was therefore selected for subsequent systematic investigation. To establish a more comprehensive comparison and further highlight the low-temperature advantages of the designed LiDFOB + DMS/HFE/FEC electrolyte, a $LiBF_4$-based electrolyte, commonly used as a low-temperature reference salt system[36], was evaluated under identical test conditions. Supplementary Figure 13 presents the CV curves of the $LiBF_4$ electrolyte at 25 °C collected at scan rates from 0.1 to 0.5 mV $s^{-1}$, where the redox peak currents increase systematically with scan rate. The rate capability of the $LiBF_4$ electrolyte at -20 °C is summarized in Supplementary Figure 14. The discharge capacity decreases progressively as the current rate increases from 0.1 C to 0.7 C, and partially recovers when the rate is returned to 0.1 C, indicating moderate reversibility with noticeable capacity loss. Moreover, at -20 °C, the $LiCoO_2$‖Li cell using the $LiBF_4$ + PC/DME delivers an initial discharge capacity of approximately 110.3 mAh $g^{-1}$ and maintains about 89.5% capacity retention after 500 cycles at 0.2 C [Supplementary Figure 15]. While the $LiBF_4$ electrolyte exhibits reasonable cycling stability at -20 °C, its specific capacity and retention remain below those values achieved with the LiDFOB + DMS/HFE/FEC formulation under the same protocol. The $LiBF_4$ + PC/DME electrolyte was retained as a conventional low-temperature reference, whereas the newly introduced $LiBF_4$ + DMS/HFE/FEC electrolyte serves as the matched-solvent control for separating salt-specific effects from those of the solvent composition. Under the same solvent composition, the $LiBF_4$ + DMS/HFE/FEC electrolyte retains 91.23% of its initial discharge capacity after 100 cycles at -20 °C and 0.2 C [Supplementary Figure 16]. Although this result confirms that the DMS/HFE/FEC solvent environment supports subzero operation, the earlier capacity decay compared with the LiDFOB-based electrolyte indicates an additional contribution from $DFOB^-$ chemistry to long-term interfacial stability.

Beyond subzero operation, we further assessed the high-temperature performance of various electrolyte systems. Supplementary Figure 17 displays the cycling stability of $LiCoO_2$||Li cells operated at 40 °C using LiDFOB + DMS/HFE/FEC and $LiPF_6$ + EC/DMC electrolytes. The LiDFOB-based electrolyte enables highly stable cycling behavior at 40 °C, maintaining a discharge capacity of about 122.9 mAh $g^{-1}$ after 200 cycles at 1.0 C, equivalent to 100% capacity retention relative to its first discharge profile, with Coulombic efficiency consistently near 100% throughout. In contrast, the $LiPF_6$ + EC/DMC electrolyte suffers from rapid capacity fading at 40 °C, with the discharge capacity continuously dropping from 125.5 mAh $g^{-1}$ to below 44.6 mAh $g^{-1}$ after 200 cycles, translating to a mere 35.5% capacity retention. The divergence in cycling stability is further corroborated by the evolution of the corresponding galvanostatic charge/discharge profiles. For the LiDFOB + DMS/HFE/FEC cell, the charge and discharge profiles remain nearly perfectly overlapped from the 1st to the 200th cycle, showing negligible polarization growth and well-preserved voltage plateaus [Supplementary Figure 18]. The sustained overlap of the voltage profiles indicates stable interfacial kinetics and limited parasitic side reactions at elevated temperature, which is consistent with a more robust inorganic-rich interphase in the LiDFOB-based electrolyte. By contrast, the $LiPF_6$ + EC/DMC cell suffers

from progressively larger polarization with cycling, manifested by increasingly sloped discharge curves, shortened and ill-defined plateaus and a substantial loss of reversible capacity [Supplementary Figure 19].

To elucidate the role of electrolyte chemistry in governing electrode/electrolyte interphase evolution, post-cycling morphological and surface chemical analyses were performed on both composite $LiCoO_2$ cathodes and Li metal anodes recovered from cells employing the different electrolyte formulations. As shown in Figure 3A and B, compared with the pristine $LiCoO_2$ particles, the $LiCoO_2$ cathode cycled in the LiDFOB + DMS/HFE/FEC system retains a relatively smooth and dense surface morphology, coated with a thin and conformal passivation layer. This morphology suggests a more uniform and compact interphase that can promote homogeneous $Li^+$ flux across the electrode surface and reduce localized current concentration, which in turn helps mitigate parasitic reactions at the electrode-electrolyte interface. The apparent continuity and conformality of this interphase further imply enhanced mechanical integrity and chemical stability, both of which are critical for maintaining intimate electrode/electrolyte contact and accommodating volume fluctuations during repeated $Li^+$ insertion/extraction. In contrast, the $LiCoO_2$ cathode cycled in $LiPF_6$ + EC/DMC electrolyte shows irregular granular deposits and a more porous, heterogeneous surface [Figure 3C], which is characteristic of nonuniform electrolyte decomposition, resulting in a poorly passivating and mechanically fragile interphase. Furthermore, such a heterogeneous and unstable interphase is prone to continuous cracking and reformation upon cycling, a detrimental process that not only accelerates electrolyte depletion but also leads to progressive accumulation of resistive byproducts, ultimately manifesting as the severe capacity fading observed in Figure 2E and F.

XPS profiling reveals fundamentally distinct interphase chemical compositions dictated by electrolyte speciation. Figure 3D presents the high-resolution Li 1s spectra of the cycled Li-anode surfaces. In the Li 1s region, the anode cycled in the LiDFOB + DMS/HFE/FEC electrolyte exhibits a dominant LiF signal at 56.1 eV, alongside a broader Li-O component near 55.0 eV, indicating the formation of an inorganic-rich interphase on the Li surface. By contrast, the anode from the $LiPF_6$ + EC/DMC cell yields a weaker LiF contribution and a relatively stronger Li-O component, suggesting a reduced LiF fraction and a greater contribution from oxygen-containing species in the SEI. This inorganic matrix integrity is further corroborated by F 1s spectra, where the LiF content in the LiDFOB + DMS/HFE/FEC system is significantly higher than that in the conventional electrolyte [Supplementary Figure 20]. In the C 1s spectrum of Figure 3E, the anode cycled in the LiDFOB-based electrolyte shows prominent C-C and C-H signals together with a modest C-O contribution[37], demonstrating controlled decomposition of FEC and the dimethyl sulfite co-solvent (DMS) with minimal formation of polymeric or carbonate-rich byproducts. Meanwhile, the O 1s spectrum [Figure 3F] displays a pronounced low-binding-energy component assigned to metal-oxygen species, corroborating the presence of inorganic oxides that contribute to the mechanical robustness and chemical passivation of the SEI[38]. In contrast, the anode cycled in the $LiPF_6$ + EC/DMC electrolyte shows markedly enhanced organic C-O and C=O contributions, indicating that the SEI contains a larger fraction of carbonate-derived species. Such an organic-rich interphase may be more susceptible to repeated damage and repair during cycling. This continuous breakdown and repair process not only consumes additional electrolyte but also exacerbates interfacial impedance growth, particularly under the thermally and kinetically challenging conditions of low-temperature operation.

Complementing the anode analysis, XPS was also performed on the $LiCoO_2$ cathodes recovered after cycling to probe the chemical composition of CEI formed in each electrolyte. The Li 1s signal detected on the cathode surface [Figure 3G] is weaker than on the anode, consistent with distinct interphase chemistries, namely an oxidation-derived CEI on the cathode versus reduction-derived products that enrich LiF on the Li-metal anode. Deconvolution of the C 1s spectra [Figure 3H] resolves five distinct components at binding energies of 284.8, 285.8, 287.0, 288.9, and 290.7 eV, which are assigned to C-C, C-H, C-O, C=O and

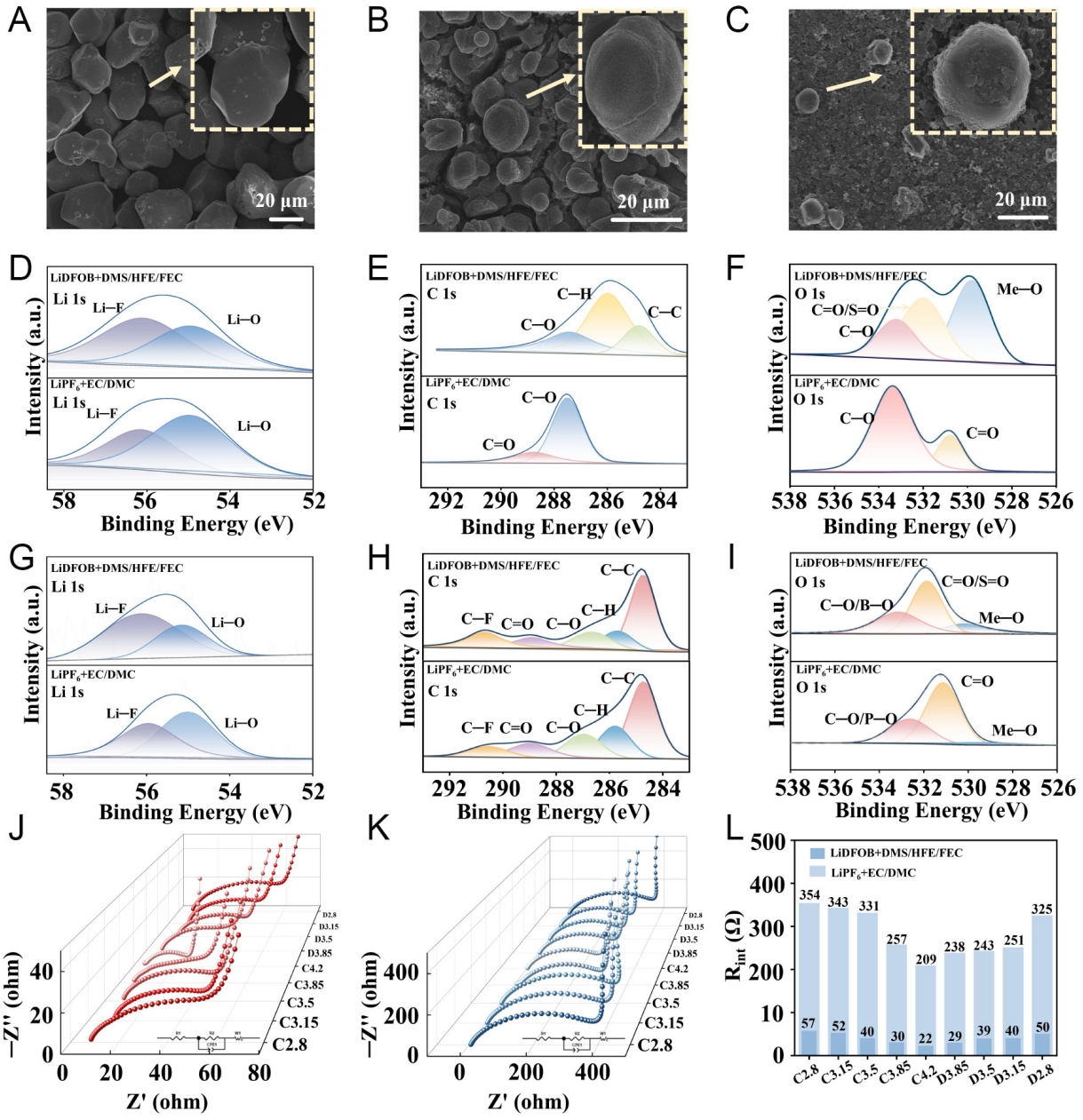


**Figure 3.** SEM images of (A) pristine $LiCoO_2$, (B) cycled $LiCoO_2$ electrode collected from cell operated in LiDFOB + DMS/HFE/FEC and (C) $LiPF_6$ + EC/DMC electrolyte. High-resolution XPS spectra of Li anodes after cycling in both electrolytes: (D) Li 1s, (E) C 1s and (F) O 1s. High-resolution XPS spectra of $LiCoO_2$ cathode after cycling in both electrolytes: (G) Li 1s, (H) C 1s and (I) O 1s. Nyquist plots of $LiCoO_2$||Li cell recorded with (J) LiDFOB + DMS/HFE/FEC and (K) $LiPF_6$ + EC/DMC electrolytes. (L) Comparison of $R_{int}$ values extracted by equivalent circuit fitting based on the EIS spectra.

C-F-related species, respectively. Compared with LiDFOB + DMS/HFE/FEC, the $LiPF_6$ + EC/DMC electrolyte shows stronger oxygenated carbon contributions in the C 1s spectra, consistent with a higher fraction of carbonate-derived organic species on the cathode surface. The O 1s spectrum of the cathode cycled in LiDFOB + DMS/HFE/FEC shows additional components, including a C-O/B-O contribution and an O=S-related feature[39], that are much less evident in $LiPF_6$ + EC/DMC [Figure 3I], suggesting the incorporation of borate- and sulfur-containing oxygen environments from $DFOB^-$ and DMS into the CEI. This assignment is further supported by the corresponding high-resolution B 1s spectra as shown in Supplementary Figure 21, which confirms the presence of boron-containing species (B-O and B-F

environments) within the CEI. Collectively, these spectroscopic features support the conclusion that the CEI chemistry of LiDFOB + DMS/HFE/FEC electrolyte contrasts with that in $LiPF_6$ + EC/DMC, where the O 1s spectrum is dominated by carbonate-derived oxygenated species and lacks the borate- and sulfur-containing signatures observed for LiDFOB + DMS/HFE/FEC.

Figure 3J and K displays the Nyquist plots of $LiCoO_2$||Li cells collected at selected charge and discharge voltages from 2.8 to 4.2 V at -20 °C. Across the entire voltage window, the semicircles in the Nyquist plots for the LiDFOB + DMS/HFE/FEC cell are substantially smaller than those for the $LiPF_6$ + EC/DMC cell, indicating a consistently lower $R_{int}$ for the designed electrolyte across all measured states. Equivalent-circuit fitting summarized in Figure 3L quantifies this difference clearly. The LiDFOB + DMS/HFE/FEC cell exhibits $R_{int}$ values ranging from approximately 22 to 57 Ω depending on the applied voltages, whereas the $LiPF_6$ + EC/DMC cell shows substantially higher $R_{int}$ values ranging from 209 to 354 Ω under identical conditions, corresponding to approximately 6.2-9.5 times higher resistance than the LiDFOB-based electrolyte. These observations are consistent with the impedance results in Figure 2C and D, which demonstrated that the LiDFOB + DMS/HFE/FEC electrolyte not only exhibits lower $R_{int}$ but also maintains a weaker temperature dependence of its interfacial kinetics. This persistently lower resistance also aligns with the XPS results, which showed a LiF-rich and inorganic-dominant SEI on the Li-metal anode together with a boron/ sulfur-containing hybrid CEI on the $LiCoO_2$ cathode in LiDFOB + DMS/HFE/FEC. Such interphases can help stabilize both electrode surfaces and preserve more favorable $Li^+$ transport pathways across the electrode-electrolyte interfaces, thereby alleviating kinetic limitations. Moreover, the anion-involved and aggregate-rich solvation structure elucidated by MD simulations and Raman spectroscopy is expected to mitigate solvent-dominated interfacial limitations and facilitate $Li^+$ transport across the electrode/electrolyte interfaces, which is consistent with the improved charge-transfer kinetics observed under high-rate and subzero-temperature conditions, as evidenced by the EIS and rate capability measurements.

To extend the investigation to a more practical configuration and elucidate the role of electrolyte chemistry in governing the performance of $LiCoO_2$||graphite full cells, post-cycling morphology and surface chemical analyses were conducted on electrodes cycled at -20 °C and disassembled at 0% state of charge. As shown in Figure 4A-C, graphite anodes cycled in the two electrolytes exhibit markedly different surface textures, highlighting the profound impact of electrolyte formulation on the integrity and uniformity of the anode interphase. The pristine graphite anode displays a typical stacked flake-like morphology with well-defined sharp edges and a relatively clean, smooth surface, providing a clear baseline without obvious surface deposits or morphological damage. In comparison, the graphite anode cycled in the LiDFOB + DMS/HFE/FEC electrolyte largely retains a recognizable flake-like morphology with clearly discernible particle boundaries together with only sparse fine deposits. The preservation of the underlying flake morphology and the absence of extensive cracking or exfoliation suggest limited mechanical degradation of the graphite particles. This observation confirms that the uniform, inorganic-rich interphase formed in this electrolyte effectively protects the anode structure during repeated $Li^+$ insertion/extraction, mitigating the volume change-induced stress that often plagues graphite electrodes. In contrast, the graphite anode cycled in the $LiPF_6$ + EC/DMC electrolyte shows much rougher surface coverage that obscures the native flake texture, together with agglomerated deposits and blurred particle edges. Such morphology suggests a more heterogeneous anode interphase and more severe parasitic reactions, which can promote local resistance buildup and accelerate the loss of effective active surface during cycling.

Sputtering-time-dependent XPS was used to examine the compositional evolution of the SEI formed on the cycled graphite anodes at sputtering times of 0, 120 and 240 s. Since sputtering-time-dependent XPS mainly reflects the relative chemical states exposed after sequential ion etching, the following discussion focuses on the compositional evolution within the probed depth region rather than an absolute layer-by-layer

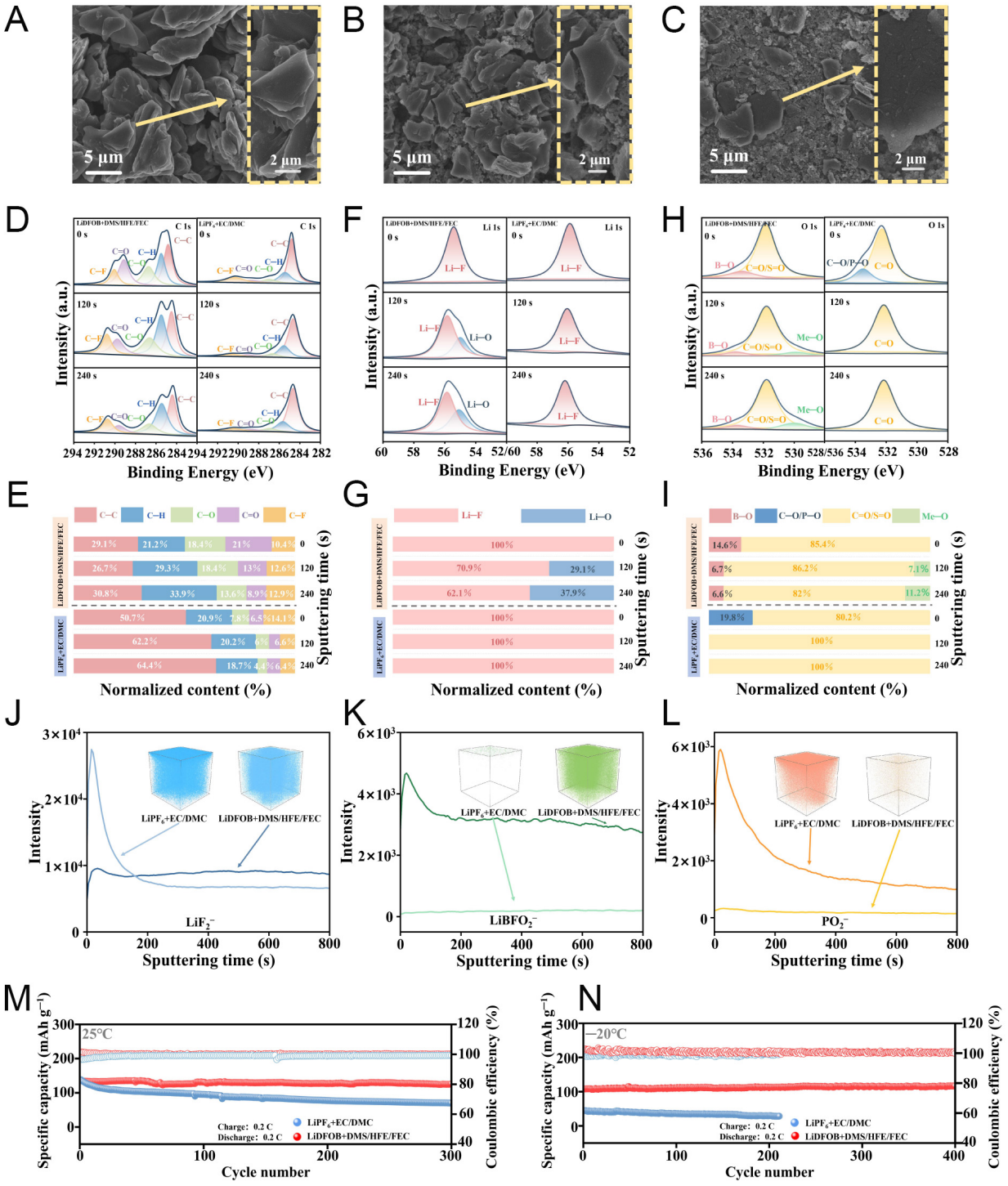


**Figure 4.** SEM images of (A) pristine graphite anode and cycled graphite anodes in (B) LiDFOB + DMS/HFE/FEC and (C) $LiPF_6$ + EC/DMC electrolytes. Depth-profiling XPS spectra of the graphite anode at different sputtering times: (D) C 1s, (F) Li 1s and (H) O 1s regions. Normalized relative contents of representative chemical bonds of graphite anodes as a function of sputtering time: (E) C 1s, (G) Li 1s and (I) O 1s. The 3D TOF-SIMS rendering images and corresponding sputtering-time profiles using different electrolytes: (J) $LiF_2^-$, (K) $LiBFO_2^-$ and (L) $PO_2^-$. Long-term cycling performance of $LiCoO_2$||graphite cells with different electrolytes (M) at 25 °C and (N) at -20 °C.

reconstruction of the SEI. As shown in Figure 4D, the C 1s spectra can be deconvoluted into components at 284.8, 285.5, 286.7, 289.2 and 290.1 eV, which are assigned to C-C, C-H, C-O, carbonyl-related species and C-F-related species, respectively, while the 284.8 eV contribution can also include graphitic carbon from the substrate. In the LiDFOB + DMS/HFE/FEC system, the relative contribution of C-C species remains lower

than that in the $LiPF_6$ + EC/DMC electrolyte throughout the sputtering process. According to Figure 4E, it stays in the range of 29.1%, 26.7% and 30.8% at 0, 120 and 240 s, respectively, for LiDFOB + DMS/HFE/FEC, compared with 50.7%, 62.2%, and 64.4% for $LiPF_6$ + EC/DMC at the same sputtering times. Coupled with the concurrently more intense signals from oxygenated and fluorinated species in the LiDFOB + DMS/HFE/FEC-derived SEI, this trend suggests that the graphite interphase is less dominated by hydrocarbon-like carbon. At the corresponding sputtering times, the $LiPF_6$ + EC/DMC-derived SEI exhibits a larger relative C-C contribution and smaller relative fractions of oxygenated and fluorinated components. Meanwhile, when combined with the weaker oxygenated and fluorinated contributions, the overall profile is consistent with a less uniform and less effectively passivating SEI on graphite along with the continued electrolyte decomposition upon cycling. Complementary TOF-SIMS measurements were used to examine the sputtering-time-dependent evolution of representative fragments within each sample, which provide semi-quantitative depth-dependent distributions of representative organic fragments across the SEI rather than relying only on the outermost surface signal. As shown in Supplementary Figure 22, the total-ion-normalized $C_2H_5O^-$ signal in the LiDFOB + DMS/HFE/FEC-derived interphase, taken here as a representative solvent-derived organic species[40], is relatively pronounced during the initial sputtering stage and attenuates rapidly with continued sputtering, consistent with a predominantly surface-associated contribution within this sample. In the $LiPF_6$ + EC/DMC-derived interphase, the normalized $C_2H_5O^-$-related signal attenuates more gradually and remains detectable over a longer sputtering interval within that sample, indicating that solvent-derived organic species remain detectable over a larger sputtering depth within the interphase. This behavior reflects a less sharply stratified SEI and a weaker separation between an organic-rich outer region and a more passivating inner layer.

The sputtering-time-dependent Li 1s spectra [Figure 4F] further reveal changes in the relative contributions of lithium-containing species over the probed sputtering interval, complementing the C 1s analysis and serving as a bridge to the subsequent discussion of the O 1s spectra. In the SEI formed in the LiDFOB + DMS/HFE/FEC electrolyte, LiF remains the predominant lithium-containing species within the probed sputtering depth, whereas the relative proportion of the Li-O fraction increases progressively with depth from 0% at the surface (0 s) to 29.1% after 120 s of sputtering and further to 37.9% at 240 s [Figure 4G]. This depth-dependent compositional evolution reveals a well-stratified SEI architecture in which LiF is present from the outer surface to the interior, while Li-O-containing species become increasingly prominent toward the inner region. Such a vertically graded structure, featuring a continuous distribution of inorganic species throughout the probed depth, is characteristic of a stable, effectively passivating interphase that can facilitate uniform $Li^+$ transport and withstand repeated cycling. The depth-dependent F 1s spectra in Supplementary Figure 23 elucidate the chemical state and spatial distribution of fluorine-containing species within the SEI formed in each electrolyte. In the LiDFOB + DMS/HFE/FEC-derived SEI, the F 1s signal appears to remain dominated by LiF across the probed depth, whereas the higher-binding-energy fluorinated contribution is relatively minor and corresponds to B-F/C-F overlapping species [Supplementary Table 4]. For the SEI derived from $LiPF_6$ + EC/DMC, a distinct P-O-F/C-F component is observed on the outer surface and rapidly decreases during sputtering. As these surface-enriched organic fluorinated species are progressively removed, the relative contribution of the LiF component within the F 1s envelope becomes more pronounced. However, this relative increase does not imply an absolute enrichment of LiF at longer sputtering times. Complementary TOF-SIMS provides semiquantitative information on the persistence of LiF-related fragment signals during sputtering. The O 1s depth profiles shown in Figure 4H further reveal complementary insights into the distribution of oxygen-containing inorganic and organic species within SEI formed in the two electrolyte systems. In the LiDFOB + DMS/HFE/FEC electrolyte, the outermost SEI region is dominated by C=O/S=O-related oxygen species. As sputtering proceeds, the Me-O contribution increases from undetectable at 0 s to 7.1% at 120 s and 11.2% at 240 s [Figure 4I], indicating an increasing contribution from inorganic oxygen-containing species toward the inner SEI. Notably, a distinct B-O component is

resolved in the O 1s spectra of the LiDFOB + DMS/HFE/FEC-derived SEI, supporting the incorporation of borate-containing species associated with $DFOB^-$ decomposition at the graphite interface. More importantly, this B-O fraction decreases from 14.6% at the surface to 6.7% at 120 s and 6.6% at 240 s, indicating that borate-containing species are mainly enriched in the surface-to-intermediate sputtered regions of the SEI. The decrease in the B-O contribution together with the progressive increase in the Me-O component suggests a graded inorganic organization, in which borate-containing species are more enriched in the outer to middle regions while Li-O-containing species become relatively more pronounced at larger sputtering depth. When considered together with the LiF-rich Li 1s profile, these results support a cooperative inorganic framework rather than a random accumulation of decomposition products. This gradient inorganic framework, with its depth-dependent compositional variation, is expected to improve the mechanical coherence and chemical resilience of the interphase, which can help the graphite anode better tolerate repeated cycling and suppress continued electrolyte decomposition. This interfacial organization therefore provides a plausible structural basis for the improved long-term cyclability of $LiCoO_2$||graphite full cells using LiDFOB + DMS/HFE/FEC, especially under low-temperature conditions.

Complementing the XPS depth profiling, TOF-SIMS analysis of the $LiF_2^-$ fragment was performed to further evaluate the depth distribution of LiF-related inorganic species within the SEI. For the $LiPF_6$ + EC/DMC-derived SEI, the apparent increase in the relative LiF contribution after sputtering mainly arises from the rapid attenuation of surface-enriched organic fluorinated species, such as C-F, rather than from an absolute enrichment of LiF in the inner SEI. This interpretation is supported by the TOF-SIMS result in Figure 4J, where the $LiF_2^-$ signal decreases rapidly with sputtering time, indicating that LiF-related species are mainly concentrated in the outer region and become progressively depleted toward the inner SEI. This attenuation is consistent with a less persistent LiF-related fragment response during sputtering, rather than a depth-persistent LiF-rich inorganic framework. In contrast, the LiDFOB + DMS/HFE/FEC-derived SEI maintains a much more stable $LiF_2^-$ signal throughout the sputtering process, demonstrating that LiF-related inorganic species are more uniformly distributed across the SEI. Such a continuous LiF-containing framework can provide more effective interfacial passivation and mechanically robust $Li^+$ transport pathways, thereby contributing to the improved low-temperature cycling stability. Moreover, the anion-specific TOF-SIMS signals in Figure 4K and L indicate markedly different anion-derived contributions to SEI formation on graphite for the two electrolytes. In LiDFOB + DMS/HFE/FEC, the $LiBFO_2^-$ signal remains comparatively elevated and persists over the sputtering duration, indicating that borate-related species derived from the anion are not merely surface-adsorbed but are integrally incorporated into the SEI matrix, forming a continuous, depth-persistent inorganic framework that reinforces the interphase. By contrast, $LiPF_6$ + EC/DMC system shows a markedly stronger $PO_2^-$-related signal, consistent with phosphorus-containing species generated from $LiPF_6$-derived decomposition chemistry. The progressive decrease of this signal with sputtering time suggests that phosphorus-containing species are enriched near the outer surface and become much less abundant at greater depth, rather than forming a depth-persistent inorganic network. This spatial confinement is consistent with more heterogeneous interphase formation in $LiPF_6$ + EC/DMC, which in turn is associated with weaker passivation and reduced interfacial stability on graphite during prolonged cycling. The depth-resolved XPS results for the cycled $LiCoO_2$ cathode further clarify the electrolyte-dependent compositional evolution of the cathode interphase in the two electrolyte systems. The C 1s depth profiles [Supplementary Figure 24] show that C-C and C-H components dominate at all sputtering depths in both electrolytes. However, these features cannot be attributed solely to CEI-derived organics because they may also include contributions from conductive carbon and other carbon-containing constituents in the composite cathode. The O 1s spectra in Supplementary Figure 25 further show that, for LiDFOB + DMS/HFE/FEC, the Me-O component becomes progressively more evident with sputtering, while the organic C-O and C=O signals concurrently attenuate. This trend is consistent with reduced organic coverage and increasing contribution from inorganic oxygen environments at larger sputtering depths, which may

arise from both inner CEI species and progressive exposure of the underlying $LiCoO_2$ lattice. In the $LiPF_6$ + EC/DMC case, however, appreciable C-O and C=O contributions remain detectable even at larger sputtering depths, indicating a more persistent organic-rich CEI and a slower transition from interphase-derived oxygen species to substrate-related Me-O environments than in LiDFOB + DMS/HFE/FEC. Li 1s depth profiling in Supplementary Figure 26 further supports this trend. For LiDFOB + DMS/HFE/FEC, the Li 1s spectra evolve from surface LiF dominance to a mixed LiF and Li-O character at larger sputtering depths, which is consistent with reduced overlayer coverage and increasing contribution from inner interphase species or the underlying $LiCoO_2$ lattice. In contrast, the Li 1s spectra of $LiPF_6$ + EC/DMC remain predominantly LiF-like across the probed depth and do not show a comparably resolved Li-O contribution, indicating that the cathode surface remains covered by a more persistent overlayer and undergoes a slower transition toward substrate-related oxide environments. Overall, the depth-resolved XPS analysis of the cycled cathode supports a more clearly differentiated cathode interphase in LiDFOB + DMS/HFE/FEC, with a relatively organic-rich outer region and increasing inorganic or oxide-like contributions at greater depth.

Together, this cathode interphase architecture and the robust graphite-anode SEI establish synergistic stabilization of both electrode-electrolyte interfaces, collectively supporting the exceptional low-temperature durability and long-term cycling stability demonstrated by the LiDFOB + DMS/HFE/FEC-based full cells. The long-term cycling stability of $LiCoO_2$||graphite full cells was evaluated both at 25 and -20 °C to validate the practical effectiveness of the designed electrolyte under realistic operating conditions [Figure 4M and N]. The $LiCoO_2$||graphite full cells were operated within a voltage window of 2.5-4.2 V, which differs from the 2.8-4.2 V range used for $LiCoO_2$||Li half cells due to the different voltage references of the full-cell configuration. Remarkably, at -20 °C, the LiDFOB + DMS/HFE/FEC full cell delivers an initial discharge capacity of 108.1 mAh $g^{-1}$ and shows a stable activation during cycling, reaching 116.8 mAh $g^{-1}$ after 400 cycles. Interestingly, the $LiCoO_2$||graphite full cell exhibits a gradual increase in reversible capacity during the first several cycles at -20 °C. This behavior is accompanied by reduced polarization and stabilized charge-discharge profiles upon cycling [Supplementary Figures 27 and 28], indicating continuous optimization of the electrode/electrolyte interfaces. The Coulombic efficiency shows moderate fluctuations during the initial activation stage and subsequently approaches approximately 100%, without progressive deterioration or large irregular excursions [Supplementary Figure 29]. Instead, they are more consistent with progressive electrolyte wetting, interfacial stabilization, reduced polarization, and increased utilization of the existing cyclable-lithium inventory during low-temperature cycling[41,42]. In stark contrast, the $LiPF_6$ + EC/DMC system suffers from rapid capacity fading, with its capacity retention decreasing to only 64.3% after 200 cycles at 0.2 C, followed by cell failure, indicating poor durability under prolonged low-temperature cycling. In addition to the electrochemical evidence, visual observation after low-temperature storage further supports the improved chemical compatibility of the LiDFOB + DMS/HFE/FEC electrolyte with the electrode materials. As shown in Supplementary Figure 30, no obvious gas evolution is observed for the LiDFOB + DMS/HFE/FEC electrolyte after storage at -20 °C, either alone or in contact with $LiCoO_2$ and graphite electrodes, indicating suppressed parasitic reactions under subzero conditions. This observation further corroborates the interfacial stability revealed by XPS and TOF-SIMS analyses. Furthermore, the low-temperature cycling performance of the present electrolyte was benchmarked against representative recently reported LIB electrolyte systems, as summarized in Supplementary Table 5. Although the reported cell configurations and testing protocols vary among different studies, the LiDFOB + DMS/HFE/FEC electrolyte achieves highly competitive subzero cycling durability, including 95.1% capacity retention after 500 cycles in $LiCoO_2$||Li cells and stable $LiCoO_2$||graphite full-cell cycling over 400 cycles at -20 °C. Therefore, the formation of an apparent well-stratified, inorganic-rich SEI on the graphite anode and a compositionally graded hybrid CEI on the $LiCoO_2$ cathode in the LiDFOB + DMS/HFE/FEC electrolyte can effectively suppress continuous electrolyte decomposition, preserve the inventory of cyclable lithium, and maintain high Coulombic efficiency throughout extended cycling. The synergistic stabilization of both

electrode/electrolyte interfaces is particularly critical under kinetically challenging low-temperature conditions, directly accounting for the superior durability of the full cell using the designed electrolyte.

## CONCLUSIONS

In summary, this work develops a LiDFOB-based electrolyte for low-temperature LIBs through the coordinated regulation of solvation structure and anion-involved interfacial chemistry. Unlike conventional low-temperature electrolyte designs that mainly focus on improving bulk ionic conductivity or solvent fluidity, this work identifies anion-participating $Li^+$ solvation as a molecular-level handle to regulate the depth-dependent chemistry of both anode and cathode interphases. By rationally integrating the low-freezing-point polar co-solvent DMS, the fluorinated diluent HFE and FEC as a film-forming additive, the $Li^+$ coordination environment was effectively modulated toward anion participation in the primary solvation sheath, which can alleviate solvent-dominated interfacial desolvation under subzero conditions. Spectroscopic and electrochemical analyses consistently support this underlying mechanism. Depth-resolved XPS results reveal a graded inorganic organization within the graphite SEI, in which LiF persists through the probed depth, Li-O-containing species become more prominent inward, and borate-related species are enriched mainly in the outer to middle regions. Complementary TOF-SIMS depth profiling further shows that borate-related fragments remain detectable through a substantial fraction of the interphase depth in the LiDFOB-based electrolyte, in contrast to the less clearly stratified and more organic-rich SEI formed in $LiPF_6$ + EC/DMC. This graded inorganic framework can help suppress continued parasitic reactions and improve the stability of the graphite interface. Electrochemically, $LiCoO_2$||Li cells employing the LiDFOB + DMS/HFE/FEC electrolyte deliver markedly enhanced cycling stability at -20 °C. Notably, the $LiCoO_2$||Li cell using the LiDFOB + DMS/HFE/FEC electrolyte retains 95.1% of its initial discharge capacity after 500 cycles at -20 °C and 0.2 C. Under the same temperature and rate conditions, the $LiPF_6$ + EC/DMC cell delivers an initial discharge capacity of only 30.2 mAh $g^{-1}$ and retains 32.8% of this initial value before failing within 200 cycles, whereas the $LiBF_4$-based reference retains approximately 89.5% of its initial capacity after 500 cycles. Meanwhile, the improved rate capability and reduced polarization further support faster interfacial $Li^+$ transport and alleviated solvent-dominated kinetic limitations. At -20 °C, the LiDFOB + DMS/HFE/FEC full cell shows an initial discharge capacity of 108.1 mAh $g^{-1}$ and evolves to a stable capacity of 116.8 mAh $g^{-1}$ during 400 cycles, underscoring the strong low-temperature durability enabled by the designed electrolyte. Overall, this work establishes a low-temperature electrolyte design strategy that couples anion-involved solvation with compositionally graded and chemically diverse interphase formation, thereby markedly extending the cycling life of LIBs under subzero conditions.

## DECLARATIONS

### Authors' contributions

Performed experiments and wrote the manuscript: Peng, S.
Participated in study design: Zhang, B.; Zhao, Z.; Shi, M.; Li, X.; Xiao, B.; Gu, X.; Zhi, M.; Chubenko, E.; Bondarenko, V.; Bandarenka, H.; Pan, Y.; Hua, S.
Revised and edited the manuscript: Yin, Q.; Li, Z.
Secured funding and conducted the review: Sui, Y.

### Availability of data and materials

The original contributions presented in this study are included in the article and Supplementary Materials. Further inquiries can be directed to the corresponding authors upon reasonable request.

### AI and AI-assisted tools statement

During the preparation of this manuscript, the AI tool ChatGPT (version GPT-5.6) was used solely for language editing under full author supervision. The tool did not influence the study design, data collection, analysis, interpretation, or the scientific content of the work. All authors take full responsibility for the accuracy, integrity and final content of the manuscript.

## Financial support and sponsorship

This work was supported by the National Key R&D Program of China (2024YFE0108500) and the Fundamental and Interdisciplinary Disciplines Breakthrough Plan of the Ministry of Education of China (JYB2025XDXM308).

## Conflicts of interest

Pan, Y. and Hua, S. are affiliated with Guoneng Nanjing Electric Power Testing and Research Co., Ltd., while the other authors have declared that they have no conflicts of interest.

## Ethical approval and consent to participate

Not applicable.

## Consent for publication

Not applicable.



## Supplementary Materials

Supplementary Materials

## REFERENCES

1. Wei, Y.; Wang, M.; Zhang, M.; Cai, T.; Huang, Y.; Xu, M. Advancements, challenges, and future trajectories in advanced battery safety detection. *Electrochem. Energy. Rev.* **2025**, *8*, 10. DOI
2. Tang, Y.; Yang, Y.; Pan, M.; et al. Critical review of thermal reduction processes for sustainable recovery of valuable metals from cathode materials in spent lithium-ion batteries. *Adv. Funct. Mater.* **2025**, *36*, e13322. DOI
3. Liu, Y.; Zhao, Y.; Liu, J.; et al. High-entropy safe electrolyte toward industrial-level lithium-ion battery. *Energy. Storage. Mater.* **2025**, *83*, 104744. DOI
4. Meng, F.; Li, Y.; Wang, S.; et al. Grain-boundary-rich cathode enabling fast ion diffusion kinetics for low-temperature and high-rate lithium-ion batteries. *Energy. Environ. Sci.* **2025**, *18*, 4775-86. DOI
5. Xiong, Z.; Meng, F.; Chen, J.; Yang, Z.; Hu, R.; Zhu, M. Electrolyte modulation strategies towards cathode-electrolyte interphase engineering in subzero-temperature lithium-ion batteries. *Rev. Mater. Res.* **2025**, *1*, 100012. DOI
6. Fan, X.; Ji, X.; Chen, L.; et al. All-temperature batteries enabled by fluorinated electrolytes with non-polar solvents. *Nat. Energy.* **2019**, *4*, 882-90. DOI
7. Sun, J.; Yao, Y.; Cui, X.; et al. Improving low-temperature tolerance of a lithium-ion battery by a localized high-concentration electrolyte based on the weak solvation effect. *Battery. Energy.* **2025**, *4*, e20240106. DOI
8. Qu, Y.; Su, C.; Wang, L.; et al. Interface engineered electrolyte design strategy for ultralong-cycle solid-state lithium batteries over wide temperature range. *Angew. Chem. Int. Ed.* **2025**, *64*, e202506731. DOI
9. Huang, R.; Wei, G.; Wang, X.; et al. Revealing the low-temperature aging mechanisms of the whole life cycle for lithium-ion batteries (nickel-cobalt-aluminum vs. graphite). *J. Energy. Chem.* **2025**, *106*, 31-43. DOI
10. Cheng, M.; Chen, A.; Zhang, Z.; Sheng, C.; Zhou, H.; He, P. Regulating lithium intercalation/plating competition to enhance low-temperature performance of Li-ion batteries. *J. Am. Chem. Soc.* **2025**, *147*, 40776-87. DOI
11. Lei, Y.; Xu, X.; Yin, J.; et al. Regulating Li-ion solvation structure and electrode-electrolyte interphases via triple-functional electrolyte additive for Lithium-Metal batteries. *Chem. Eng. J.* **2024**, *497*, 154927. DOI
12. Piao, Z.; Gao, R.; Liu, Y.; Zhou, G.; Cheng, H. M. A review on regulating $Li^+$ solvation structures in carbonate electrolytes for lithium metal batteries. *Adv. Mater.* **2023**, *35*, 2206009. DOI
13. Zhang, X.; Zhao, D.; Quan, Y.; et al. A solid-liquid hybrid electrolyte with weak-solvated solvent to reduce $Li^+$ transfer barrier at electrode and solid electrolyte interphase. *Battery. Energy.* **2025**, *4*, e70042. DOI
14. Song, G.; Yi, Z.; Su, F.; et al. Boosting the low-temperature performance for Li-ion batteries in $LiPF_6$-based local high-concentration electrolyte. *ACS. Energy. Lett.* **2023**, *8*, 1336-43. DOI
15. Xia, Y.; Zhu, D.; Hou, W.; et al. Rational lithium salt selection principle for designing high-entropy electrolytes toward high-performance lithium metal batteries. *J. Am. Chem. Soc.* **2026**, *148*, 3538-50. DOI

16. Zhao, D.; Ding, M.; Tao, M.; et al. Advanced interfacial engineering of graphite anodes for next-generation lithium-ion batteries. *Small* **2025**, *22*, e12150. DOI
17. Lee, M. A.; Jang, H. Y.; Lee, J.; et al. Underlying mechanism of electrolyte compositional engineering based on additive solvation-structure governing solid electrolyte interphase formation in lithium-ion batteries. *Small* **2024**, *21*, 2407910. DOI
18. Holoubek, J.; Liu, H.; Wu, Z.; et al. Tailoring electrolyte solvation for Li metal batteries cycled at ultra-low temperature. *Nat. Energy.* **2021**, *6*, 303-13. DOI PubMed PMC
19. Cui, X.; Li, Q.; Chang, G.; et al. Asymmetric sulfonamide design enabling high-voltage sodium-ion pouch cells in wide temperature. *Nat. Commun.* **2026**, *17*, 4378. DOI PubMed PMC
20. Chen, Y.; He, Q.; Zhao, Y.; et al. Breaking solvation dominance of ethylene carbonate via molecular charge engineering enables lower temperature battery. *Nat. Commun.* **2023**, *14*, 8326. DOI PubMed PMC
21. Li, Y.; Huang, Y.; Han, X.; et al. Temperature-adaptive fluorine in electrolyte for lithium-metal batteries at low temperatures. *ACS. Energy. Lett.* **2025**, *10*, 3610-9. DOI
22. Han, X.; Wang, C.; Xu, L.; et al. Dilute electrolyte with vehicular aggregates for stable high-energy lithium-metal batteries. *Adv. Mater.* **2025**, *38*, e12236. DOI
23. Xu, L.; Han, X.; Sung, J.; et al. 4.5-V-class safe lithium-ion batteries with silicon-majority-graphite anodes enabled by self-limiting interphase. *Adv. Mater.* **2025**, *38*, e15562. DOI
24. Jin, C. B.; Yao, N.; Xiao, Y.; et al. Taming solvent-solute interaction accelerates interfacial kinetics in low-temperature lithium-metal batteries. *Adv. Mater.* **2022**, *35*, 2208340. DOI
25. Gu, R.; Zhang, D.; Xu, S.; et al. Thermoresponsive ether-based electrolyte for wide temperature operating lithium metal batteries. *Nat. Commun.* **2025**, *16*, 5474. DOI PubMed PMC
26. Wang, M.; Li, M.; Wu, J.; et al. Fluoroethylene carbonate-enabled gel polymer electrolyte for stable high-voltage lithium metal batteries. *Adv. Mater.* **2025**, *37*, 2502076. DOI
27. Zhang, Y.; Liu, Z.; Xiong, J.; et al. Ternary-anions-driven minimized solvent coordination for extreme condition-adaptive weakly solvating lithium-ion batteries electrolytes. *Adv. Funct. Mater.* **2025**, *36*, e29170. DOI
28. Ma, K.; Cao, Y.; Zhang, S.; et al. Exceptional rate performances of Li-rich Mn-based cathodes enabled by boron-based additives-driven self-optimized interface. *Nano. Lett.* **2024**, *24*, 8826-33. DOI
29. Yang, X.; Huang, Y.; Li, J.; et al. Understanding of working mechanism of lithium difluoro(oxalato)borate in Li||NCM85 battery with enhanced cyclic stability. *Energy. Mater.* **2023**, *3*, 300029. DOI
30. Qu, Z.; Xue, P.; Hu, X.; et al. Strongly and weakly solvating solvents co-coordinated electrolyte for stable lithium metal batteries. *ACS. Energy. Lett.* **2025**, *10*, 2913-23. DOI
31. Meng, X.; Zhang, X.; Shi, L.; et al. A competitive coordination effect to simultaneously achieve high-energy and stable cycles in a Li-metal pouch cell at -40 °C. *Energy. Environ. Sci.* **2025**, *18*, 9907-16. DOI
32. Lee, K.; Kwon, S.; Kim, J.; et al. Fluorinated cyclic ether diluent for high-voltage lithium metal batteries. *ACS. Energy. Lett.* **2024**, *9*, 2201-11. DOI
33. Hu, C.; Dai, L.; Huang, F.; et al. Carboxylate-based electrolyte with bilateral functions enable working sodium-metal batteries at -60°C. *Angew. Chem. Int. Ed.* **2025**, *64*, e202508584. DOI
34. Huang, Y.; Fang, H.; Geng, J.; Zhang, T.; Hu, W.; Li, F. Anionic solvation transition at low temperatures for reversible anodes in lithium-oxygen batteries. *J. Am. Chem. Soc.* **2024**, *146*, 26516-24. DOI
35. Zhang, Y.; Li, F.; Cao, Y.; et al. Tuning the FEC-related electrolyte solvation structures in ether solvents enables high-performance lithium metal anode. *Adv. Funct. Mater.* **2024**, *34*, 2315527. DOI
36. Qin, N.; Chen, J.; Lu, Y.; et al. Trace $LiBF_4$ enabling robust LiF-rich interphase for durable low-temperature lithium-ion pouch cells. *ACS. Energy. Lett.* **2024**, *9*, 4843-51. DOI
37. Li, G.; Jiang, H.; Kou, R.; et al. A superior carbonate electrolyte for stable cycling Li metal batteries using high Ni cathode. *ACS. Energy. Lett.* **2022**, *7*, 2282-8. DOI
38. Tran, T. N.; Cao, X.; Xu, Y.; et al. Enhancing Cycling stability of lithium metal batteries by a bifunctional fluorinated ether. *Adv. Funct. Mater.* **2024**, *34*, 2407012. DOI
39. Zhang, H.; Wu, X.; Kong, W.; et al. Tailoring electrolyte solvation of dimethyl sulfite with fluoride dominant via electrolyte engineering for enabling low-temperature batteries. *Energy. Storage. Mater.* **2025**, *74*, 103955. DOI
40. Jiang, Y.; Li, T.; Liang, Y.; Zheng, R.; Zheng, Y. Stable-cycling lithium metal batteries enabled by strategic lithium kinetics engineering. *Energy. Storage. Mater.* **2026**, *84*, 104848. DOI
41. Huang, W.; Ye, Y.; Chen, H.; et al. Onboard early detection and mitigation of lithium plating in fast-charging batteries. *Nat. Commun.* **2022**, *13*, 7091. DOI PubMed PMC

42. Han, X.; Mao, S.; Wang, Y.; et al. Manipulation of lithium dendrites based on electric field relaxation enabling safe and long-life lithium-ion batteries. *Nat. Commun.* **2025**, *16*, 3699. DOI PubMed PMC